

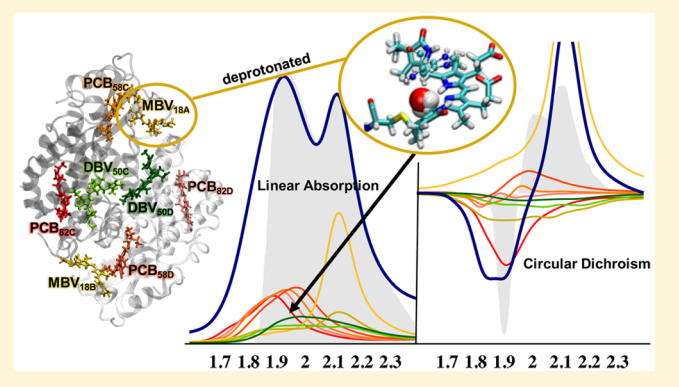
First-Principles Models for Biological Light-Harvesting: Phycobiliprotein Complexes from Cryptophyte Algae

Mi Kyung Lee, Ksenia B. Bravaya, and David F. Coker*

Department of Chemistry, Boston University, 590 Commonwealth Avenue, Boston, Massachusetts 02215, United States

Supporting Information

ABSTRACT: There have been numerous efforts, both experimental and theoretical, that have attempted to parametrize model Hamiltonians to describe excited state energy transfer in photosynthetic light harvesting systems. The Frenkel exciton model, with its set of electronically coupled two level chromophores that are each linearly coupled to dissipative baths of harmonic oscillators, has become the workhorse of this field. The challenges to parametrizing such Hamiltonians have been their uniqueness, and physical interpretation. Here we present a computational approach that uses accurate first-principles electronic structure methods to compute unique model parameters for a collection of local minima that are sampled with molecular dynamics and QM



geometry optimization enabling the construction of an ensemble of local models that captures fluctuations as these systems move between local basins of inherent structure. The accuracy, robustness, and reliability of the approach is demonstrated in an application to the phycobiliprotein light harvesting complexes from cryptophyte algae. Our computed Hamiltonian ensemble provides a first-principles description of inhomogeneous broadening processes, and a standard approximate non-Markovian reduced density matrix dynamics description is used to estimate lifetime broadening contributions to the spectral line shape arising from electronic-vibrational coupling. Despite the overbroadening arising from this approximate line shape theory, we demonstrate that our model Hamiltonian ensemble approach is able to provide a reliable fully first-principles method for computation of spectra and can distinguish the influence of different chromophore protonation states in experimental results. A key feature in the dynamics of these systems is the excitation of intrachromophore vibrations upon electronic excitation and energy transfer. We demonstrate that the Hamiltonian ensemble approach provides a reliable first-principles description of these contributions that have been detailed in recent broad-band pump-probe and two-dimensional electronic spectroscopy experiments.

INTRODUCTION

The nonequilibrium dynamics of the earliest steps of biological photosynthetic light harvesting, and how excited state coherent nuclear and electronic motions play roles to enhance the efficiency of excitation energy transfer and charge separation, has been a subject of extensive study for the past decade. This has been made possible by considerable progress in the development of experimental techniques such as nonlinear 2D electronic spectroscopy (2DES) and broad-band pump-probe spectroscopy¹⁻⁵ that can probe the average ultrafast dynamics of an initially prepared ensemble of electronically and vibrationally excited superposition states.⁶⁻¹⁰ These experimental techniques can now explore the fundamental quantum dynamics responsible for the core steps of these processes and have revealed a remarkable richness in this underlying early time evolution. ^{11–19} Understanding how nature optimizes the short time nonequilibrium dissipation and dephasing processes to control the ultimate charge separation efficiency is a key design concept that these experiments can now begin to address, but generally only in the inhomogeneously broadened,

ensemble-averaged limit. Detailed knowledge of the underlying molecular design criteria that make these natural systems so efficient will be transformative, potentially enabling significant advances in solar energy technologies. 20-27 Unfortunately, exploring how particular instantaneous inherent structures²⁸⁻³² sampled by fluctuations might do much better (or much worse) than the average as far as efficiency is concerned is not possible with these current experimental techniques.³³

Theory has also come a long way on some of the different fronts needed to help understand and interpret the results of these experiments. 34-36 For example, given a parametrized model Hamiltonian for the multichromophore electronic subsystem linearly coupled to a harmonic bath, there are now a variety of approximate methods and even some tractable exact approaches^{37–44} that can treat the dynamics and extract reliable spectroscopic signals.

Received: February 20, 2017 Published: May 18, 2017

The semiempirical global model optimization approach attempts to parametrize these sorts of models by fitting large sets of available ensemble averaged experimental data as well as incorporating some computed results. 11,12,45-47 But how useful such, in general nonunique, averaged descriptions with their limited treatment of fluctuations and inherent assumptions about time scale separations can be for providing realistic physical interpretations of the underlying physical processes and mechanisms remains questionable.

One approach to overcome this issue is to use advanced quantum chemical theoretical methods to accurately probe energetic fluctuations and correlations that underlie the microscopic dynamics of these systems and to provide a better representation based on an ensemble of accurate, instantaneous dynamical model Hamiltonians. If these calculations are sufficiently reliable we should be able to pick apart the ensemble average description and focus on the behavior of subensembles of structures that highlight highly efficient processes hidden by the ensemble average and so expose optimal nanoscale design principles. Exactly how to accomplish such a first-principles route to gaining this microscopic understanding has been the subject of considerable research, 48-53 but given the sheer size and complexity of these systems a generally reliable, robust, and predictive approach has remained elusive.

In this paper, we lay the foundation for validating such computational methodology and thus present a theoretical framework capable of generating ensembles of accurate model Hamiltonians that should be applicable to general photosynthetic light harvesting systems. For the purpose of demonstrating our model Hamiltonian ensemble parametrization approach, we will focus on predicting the results of electronic spectroscopy experiments such as absorption and circular dichroism that are determined principally by short time quantum dynamical behavior that can often be reliably described by Redfield theory and related approximate methods, 54-57 though alternative approaches that incorporate non equilibrium nuclear and electronic wave packet dynamics will in general be crucial for providing accurate descriptions of the full early time, nonlinear and transient response.

The approach developed here involves running long molecular dynamics (MD) trajectories using molecular mechanics (MM) force fields to sample conformational fluctuations that may occur during experimental averaging. Though the reliability of the details of these MM force fields can be questionable, ^{58–60} we expect such trajectories to provide a reasonable sampling of qualitative equilibrium fluctuations. This is the same starting point that has been employed in much of the previous published work that attempts to use firstprinciples based approaches to study these systems. $^{52,61-65}$ The procedure we present here, however, is fundamentally different since we avoid the inconsistency associated with directly using the configurations sampled from the approximate MM model ground state surface in electronic structure calculations to compute the Franck-Condon excitation energies.⁶⁶ Rather, we only use the sampled MM configurations to initiate QM ground state optimization of chromophore geometries in the presence of the instantaneous local fields provided by the MM partial charges of the surrounding protein environment to locate the "inherent structures" of the chromophores. This terminology, "instantaneous, inherent structures", was first coined by Stillinger et al. and in our application refers to the pigment-protein configurations corresponding to all the local

minima of the potential energy surface. 67-70 Thus, a single complex will slowly change from one inherent structure or configuration to another as long as enough thermal energy is available to overcome the transition barrier.

Ground and excited state properties are then computed at these optimized geometries to parametrize an ensemble of instantaneous local system-bath model Hamiltonians that can be incorporated in model studies of the vibrational and vibronic relaxation processes. Alternatively, one can exploit QM/MM MD^{71,72} approaches for sampling configurational space, as has been done recently for some of the light harvesting systems we study here. 68,73 However, efficient exploration of the potential energy surfaces becomes prohibitively expensive with such approaches, compared to the method we describe here.

It is interesting to note that when the standard electronic embedding QM/MM protocol, in which the system is partitioned into the region to be described quantum mechanically in the presence of the electric fields arising from the fixed partial charges of the MM environment, has been applied to compute excitation energies of photoactive proteins, several studies have reported significant discrepancies with experimental results. 66,74-79 This could result from inadequate treatment of the QM subsystem, but another contributing factor could be the local polarization of the environment due to the presence of the QM charge distribution that cannot be captured by a fixed partial charge description. This environmental polarization can be accounted for, for example, with polarizable embedding methods. 80,81 With such approaches, different charge distributions in the ground and excited states of the QM region will polarize the environment in different ways resulting in effectively different local environments for the different electronic states of the QM subsystem. The polarized environment and QM region charge distributions must be converged self-consistently, and the different environmental polarizations will produce different shifts in excitation energies. If the charge distributions of the ground and excited states are not very different, however, this higher order environmental polarization effect will be small. In the calculations reported here we have neglected environmental polarization, as it is of higher order than the other effects we consider explicitly in our calculations. This is consistent with the findings of other recent studies on photosynthetic light harvesting systems.⁸² We will show that a more significant contribution to predicting spectral band positions and line shapes comes from the accurate description of the chromophore vibrational reorganization energy upon electronic excitation.

Phycobiliproteins. As a concrete example we demonstrate our approach for two experimentally well-characterized phycobiliprotein complexes found in unicellular cryptophyte algae that uniquely employ methine-bridged linear tetrapyrrole, or bilin, molecules to harvest and transfer solar energy in the form of molecular electronic excitation to the Photosystem II complex where charge separation is initiated. This versatile class of pigment-protein systems provides an ideal testing ground for our first-principles methods, as different organisms are known^{83,84} to mix and match different types of chromophores in the different available protein environments within the same basic structural subunits to achieve desired energy flow patterns.

Two very different and well-studied phycobiliprotein structures are the Phycoerythrin 545 (PE545) complex from Rhodomonas CS24⁴⁵ and the Phycocyanin 645 (PC645) complex from Chroomonas CCMP27084 that, as presented in

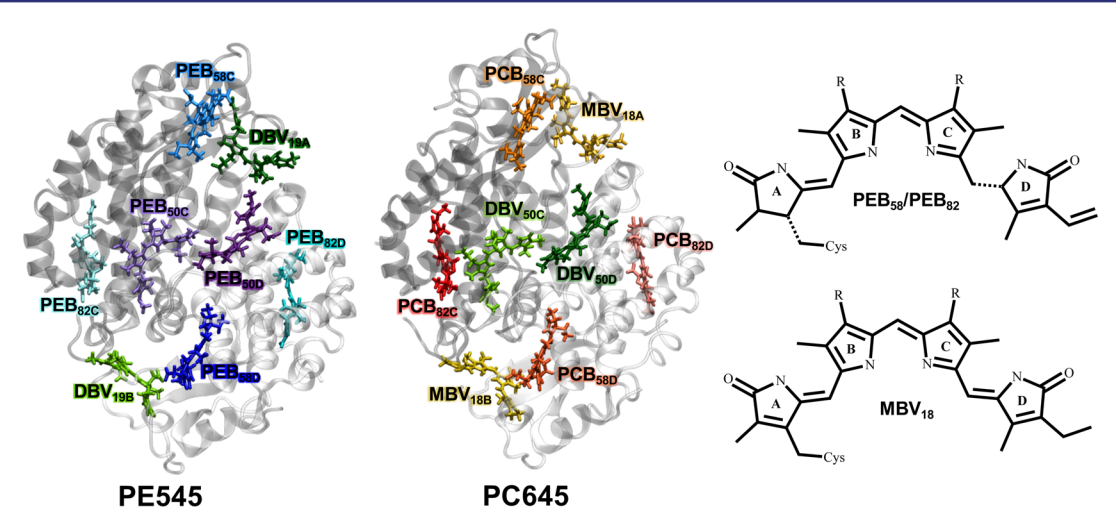


Figure 1. Two representative pigment (right panel) and pigment-protein complex (left panel) structures for phycobiliproteins PE545 and PC645.

Figure 1, covalently bind eight bilins to conserved cysteine sites in the pseudosymmetrically arranged $\alpha_1\beta$ and $\alpha_2\beta$ subunits. At about 2 nm, the average interchromophore distances in these systems are nearly twice as large as the typical interchromophore distances found in chlorophyll-based pigment—protein complexes. The central bilin pair at the dimer interface is the exception, where, for these chromophores, the distance between the two nearest pyrrole rings is about 0.5 nm and results in strong electronic coupling between these chromophores.

Though the protein scaffolds of the PE545 and PC645 complexes are nearly identical, the chromophore compositions are different, and the chromophores differ in their π conjugation lengths. The differences in chromophore structure and the local environments of these molecules further result in the 100 nm shift in mean absorption wavelength of the complexes. In PE545, there are only phycoerythrobilin (PEB) and dihydrobiliverdin (DBV) chromophores, which in Figure 1 are labeled by the residues to which they are bound. The complex forms a multidirectional energy funnel in which the central chromophores at the interface between the dimer of dimers (position 50) have the highest energies and act as the "sources" for excitation energy transfer, while those near the periphery provide the lower energy transient and "sink" states. In PE545, for example, the lowest energy states are often localized on the peripheral DVB₁₉ chromophores. For the PC645 complex, which functions at lower absorption energy, the DBV molecules now reside at the dimer interface and play the role of the source states, while the phycocyanobilin (PCB) and the mesobiliverdin (MBV) molecules form lower energy intermediate and sink states. 14,85,80

All eight bilins in both complexes strongly interact with the local protein environment. In particular, with the exception of the two DBV_{19} and two MBV_{18} bilins in PE545 and PC645 respectively, the nitrogens in the central B and C pyrrole rings (two representative chromophore structures are displayed in the right panel of Figure 1; all chromophore structures are given in the Supporting Information) are coordinated to aspartic acid residues. This interaction stabilizes the protonated form of the nitrogens in the B and C pyrrole rings so that all four nitrogens are assumed to be protonated giving rise to a net charge of +1 along the π -backbone. Together with the two negatively charged propionic groups (indicated as R groups in right panel of Figure 1), the bilins have a zwitterionic-like

character with a net charge of -1. For the DBV_{19} and MBV_{18} bilins, on the other hand, the two central nitrogens are coordinated with a water molecule (these interactions are shown in Figure 3 and detailed in the Supporting Information) and the protonation states remain ambivalent for the bilins at these 18/19 positions. In a stringent test case study we will explore the influence of protonation/deprotonation at the MBV_{18} site in PC645 on the spectroscopy and function of this complex.

Model Hamiltonian Ensemble. With our approach, each ground state energy basin sampled by the MD trajectory is characterized by the quantum chemical properties of the "inherent structures" of the chromophores. The inherent structures are generated by QM/MM geometry optimization of each bilin in its instantaneous local MM environment, and its properties are defined by (i) the ground state normal modes; (ii) the electronic excitation energy; (iii) the excited state gradients at the Franck-Condon point; and (iv) the transition dipole moments the chromophores that determine their electronic coupling. Details of these calculations are presented in the Supporting Information. These computed local attributes of the ground and excited states of each chromophore are sufficient to determine the parameters in a Frenkel-exciton model Hamiltonian (the form of which is given in the Supporting Information) for each sampled inherent structure. Such models are ubiquitous in the theory of EET in lightharvesting complexes and describe the relevant degrees of freedom including (i) the electronically excited states of the donor and acceptor chromophores and their electronic coupling and (ii) the coupling of these electronic states to the harmonic, nuclear degrees of freedom that are involved in the dissipative energy transfer dynamics. The latter component of the Hamiltonian is divided into two parts: the lowerfrequency continuum of modes that describe the collective motion of the protein-solvent environment; and the discrete, higher frequency modes associated with the internal vibrations of the individual chromophores. These vibrational modes are assumed to be in thermal equilibrium before photon absorption and, after the electronic excitation, will relax in response to the modified electronic distribution of the excited chromophores. The forces exerted on the nuclei in the different electronic states will drive the nonequilibrium EET process, and these electronic-nuclear couplings are quantified by the modedependent reorganization energies and summarized in the

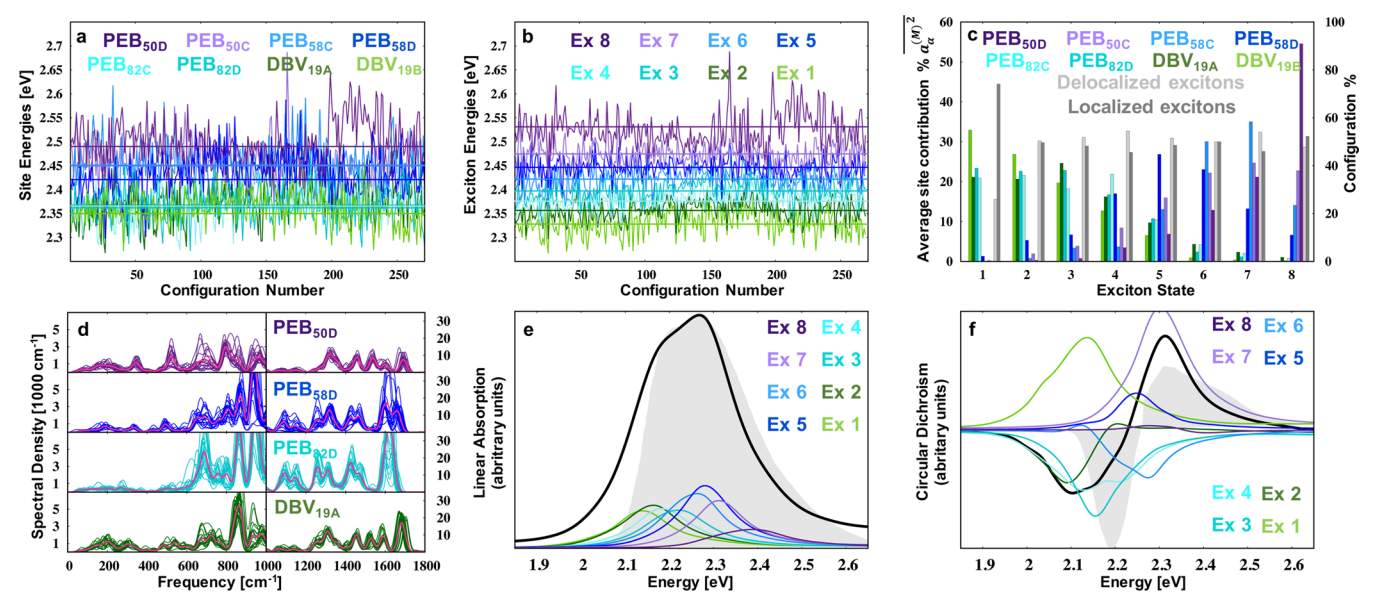


Figure 2. (a) Configuration-dependent site energies and mean site energies values (horizotonal lines) of different chromophores labeled using the same color scheme as Figure 1. (b) Configuration-dependent exciton energies computed from the site Hamiltonians. (c) Exciton state ensemble average compositions and localization characteristics. For each exciton the color coded left bars give the average populations of the different chromophore site states (left axis scale), while the right-hand dark-gray and light-gray bars give the percentage of ensemble members that have localized/delocalized eigenstates as specified by the right axis scale. (d) Instantaneous intramolecular spectral densities for bilins DBV_{19A}, PEB_{82D}, PEB_{58D}, and PEB_{50D}. Pink curve gives ensemble average spectral density. Note scale changes in left and right subpanels. (e) Simulated linear absorption spectrum at 298 K (black line) compared with the experimentally measured spectrum at room temperature (filled gray). In addition, the average excitonic contributions to the overall computed spectrum are shown with colored lines. (f) Simulated circular dichroism spectrum (rotatory strength) at 298 K (black line) compared with the experimentally measured spectrum at room temperature (filled gray), as well as the average excitonic contributions shown with colored lines.

resulting spectral densities. Mathematical details of the model^{66,87} and how we use it in the computation of approximate linear spectroscopy signals are presented in the Supporting Information.

■ RESULTS AND ANALYSIS

Analysis of PE545 Results. In Figure 2a, the configuration-dependent site energies fluctuating about the mean site energies (horizontal lines) are shown. The ordering of the mean site energies are in agreement with empirical studies 12 that have assigned larger site energy values for PEB₅₀ and PEB₅₈ bilins relative to the PEB₈₂ and DBV₁₉ bilins. This site energy difference between the chemically identical PEB₈₂, PEB₅₈, and PEB₅₀ molecules arise from the differences in the bilin equilibrium conformations adopted in the protein environment. Both PEB58 and PEB50 have significant torsional distortion about the allylic bond connecting pyrrole rings A and B due to hydrogen-bonding with the local environment. 45,88 This torsional twist, which weakens the π -conjugation that extends through the pyrrole chain, is significantly less for PEB₈₂ due to fewer hydrogen-accepting groups in the local environment. Thus, the PEB₈₂ molecules, with the longest "effective π conjugation" among the PEB molecules, have the smallest vertical transition energies, so that their site energies are comparable to those of the DBV₁₉ molecules that have longer conjugation lengths due to an additional double bond in pyrrole ring A.45,76

From configuration to configuration, the site energy gaps and orderings deviate significantly from the mean site energies and ordering. These variations are easily observed for the highest site that alternates between the different PEB₅₀ and PEB₅₈ molecules and the lowest site that fluctuates between the

various PEB₈₂ and DBV₁₉ molecules. By comparison, the offdiagonal electronic couplings between pairs of sites do not fluctuate significantly (tabulated in the Supporting Information), validating the Condon approximation. The variation in the exciton energies, obtained by diagonalizing the instantaneous site Hamiltonians, shown in Figure 2b, thus arises mainly from the changes in the eight site energies of each configuration. Compared to the mean site energy gaps, the average energy gap between successive exciton states are approximately uniform due to excitonic splitting induced by moderately strong electronic couplings. From sampled configuration to configuration, the instantaneous excitonic gaps vary significantly such that energy transfer rates and mechanisms may differ for each ensemble realization. For energy transfer between states with small energy gaps, the quasi-resonant low-frequency nuclear modes of the chromophore, protein, and solvent environment with strong electronicnuclear couplings drive the dissipative dynamics from high to low energy exciton states. For EET dynamics between states with larger energy gaps, localized, higher frequency intramolecular vibrational modes of the bilins need to be strongly coupled to the electronic states to facilitate this energy transport.

The distributions of electronic-nuclear couplings are summarized in the calculated spectral densities shown in Figure 2d. Following the prescription outlined in earlier work, 66 the intramolecular contributions to the spectral densities have been computed for 20 independent configurations and are shown as overlapping colored curves for four representative sites (all eight in the Supporting Information); the averaged spectral densities are shown as dark-pink lines in the four subpanels. These intramolecular spectral densities correspond

to total reorganization energies 66 of 1155 cm $^{-1}$ for PEB $_{\rm 50D}$ and 2150 cm $^{-1}$ for PEB $_{\rm 82D}$, for example, where these values are 5–10 times larger than typical representative values of \sim 200 cm $^{-1}$ for bacteriochlorophylls (e.g., in FMO $^{\rm 89,90}$). For all eight sites, the intramolecular vibrational modes in all frequency ranges can be strongly coupled to the electronic states. In the low frequency region, magnified on the left side of Figure 2d, the electronic-nuclear coupling for the intramolecular modes is estimated to dominate over that arising from couplings with the intermolecular modes of the protein and solvent environment. Thus, the total spectral densities are accurately approximated by only their intramolecular contributions across the whole frequency range. As detailed in previous work 87,91 this is not the case in chlorophyll systems where the inter- and intramolecular couplings can be of comparable magnitudes.

The differences in the spectral densities for the various PEB sites reflect the variation in the equilibrium bilin geometries influenced by the interactions with the different local protein environment. For each site, modes with frequencies ranging from 600 to 800 cm⁻¹ show noticeable dispersion in spectral density amplitudes. These intramolecular vibrational modes are associated with the methine torsional and the methine-bridged hydrogen out-of-plane (HOOP) modes. Since the main difference between the optimized configurations are the equilibrium torsional geometries, significant variations are expected for these modes, as configurations slowly fluctuate from one local inherent structure minimum to another. The higher frequency bimodal peaks above 1600 cm⁻¹ have been assigned to localized C=C and C=N stretching modes in previous Raman studies.

While the rate of energy transfer will depend significantly on the spectral densities, the pathways will be dominated by the nature of the exciton states. Because of the fluctuating site energy ordering, the composition of the exciton states, as well as the extent of excitation delocalization over multiple sites, will differ for each realization of the inherent structure Hamiltonian. In Figure 2c we see that, in approximately 50% of sampled configurations, the exciton states 2 through 8 are delocalized states typically involving 2-3 chromophores. The remaining half are localized such that only one site is electronically excited. Only for the lowest exciton state 1 do we find that the majority (>70%) of configurations yield localized states. In this lowest energy excitonic state, however, the locally excited bilin varies from configuration to configuration as can be seen by analyzing the averaged percentage site contribution to exciton state 1. From the results in this panel we see that, either of the PEB₈₂ molecules, or either of the pair of DBV₁₉ molecules, (i.e., four different localized states), can act as the final energy acceptor in this complex. For higher exciton states, the contribution from these four lowest sites steadily decrease and the contribution from the PEB₅₀ and PEB₅₈ molecules increase. By exciton state 8, PEB_{50D} noticeably contributes to this highest exciton state more frequently than the remaining bilins. Because of these variations in the site contribution (excitation), there will be no one unique EET pathway, but multiple pathways that flicker on and off as the system explores its different inherent structure

All realizations contribute to the averaged linear absorption, and exciton-coupled circular dichroism (ECCD) spectra shown in the last two panels, Figure 2e and Figure 2f. These spectra have been computed for 298 K and are compared with the experimentally measured room temperature spectra presented as the filled-gray curves. The inhomogeneous contribution to

the line shape is obtained from the ensemble of Hamiltonians sampled from the inherent structure configurations. The oscillator and rotatory strengths used to calculate the contributions to these spectra for the different configurations have been computed with transition dipoles obtained for each site and are related to the excitonic optical response functions as summarized in the Supporting Information. The homogeneous broadening has been approximated using our calculated spectral densities within the limits of Redfield theory. Hus, while the simulated relative peak positions at approximately 2.26 and 2.21 eV reproduce the experimental peak positions and shape, the wings of the line shape are overbroadened particularly for the lower energy region as a result of the limitations of this simple, but intuitive approximate theory.

The average exciton state contributions to the overall absorption spectrum are also analyzed in Figure 2e. The lower energy exciton states, excitons 1 through 4, with their smaller oscillator strengths, contribute to the lower energy shoulder near 2.21 eV while the higher energy and stronger oscillator strength exciton states 5 to 7 contribute to the main absorption peak at 2.26 eV. By comparison, exciton 8 shows a relatively broad weak response that contributes to the high energy tail. The relative peak positions, obtained from Redfield theory, will be shifted from the excitonic vertical transition energies by approximately the exciton reorganization energies (see Supporting Information for details of our implementation). The relative differences in the absorption intensities of these exciton states intricately depend on the transition dipoles of the populated sites, and the magnitudes and signs of the expansion coefficients $\{a_{\alpha}^{(M)}\}$ that are computed for each individual inherent structure configuration. For exciton states composed of sites with strong electronic-nuclear couplings, the averaged line shape will be significantly inhomogeneously broadened and result in decreased peak amplitudes. Thus, the smaller absorption intensities for the four lowest exciton states may arise in particular due to the PEB₈₂ bilins that exhibit the largest total reorganization energies and largest fluctuations in these quantities. Of all eight exciton states, the weakest absorption peak is observed for exciton 8 due to the dark states arising from the out-of-phase combinations from the different sites as determined by the exciton eigenvector components.

Unlike the absorption spectrum, the distinct excitonic CD signals apparent in Figure 2f—the positive band near 2.31 eV and the negative feature near 2.19 eV—cannot be cleanly attributed to specific exciton states due to significantly overlapping and often opposite-signed, excitonic contributions. It is however evident that the positively signed peak arises mainly from exciton state 7 with amplitude attenuated by other exciton states; the negatively signed peak is roughly due to incomplete cancellation of signals from exciton states 1 through 4. The computed zero-crossing point is red-shifted relative to the experimental measurements, but the general position and shape of the calculated band is in reasonable qualitative agreement though the calculated band shape is excessively broadened to lower energies. More accurate simulation of the spectral line-broadening will influence the cancellation of the oppositely signed signals and should provide better agreement with experiment. Of the eight states, exciton state 1 is a localized state for a significant number of configurations and is thus expected to have the weakest intensity. However, the opposite is observed where the overall signal is strong and very broad. All the delocalized configurations for this lowest exciton state are characterized by the in-phase combination of PEB₈₂

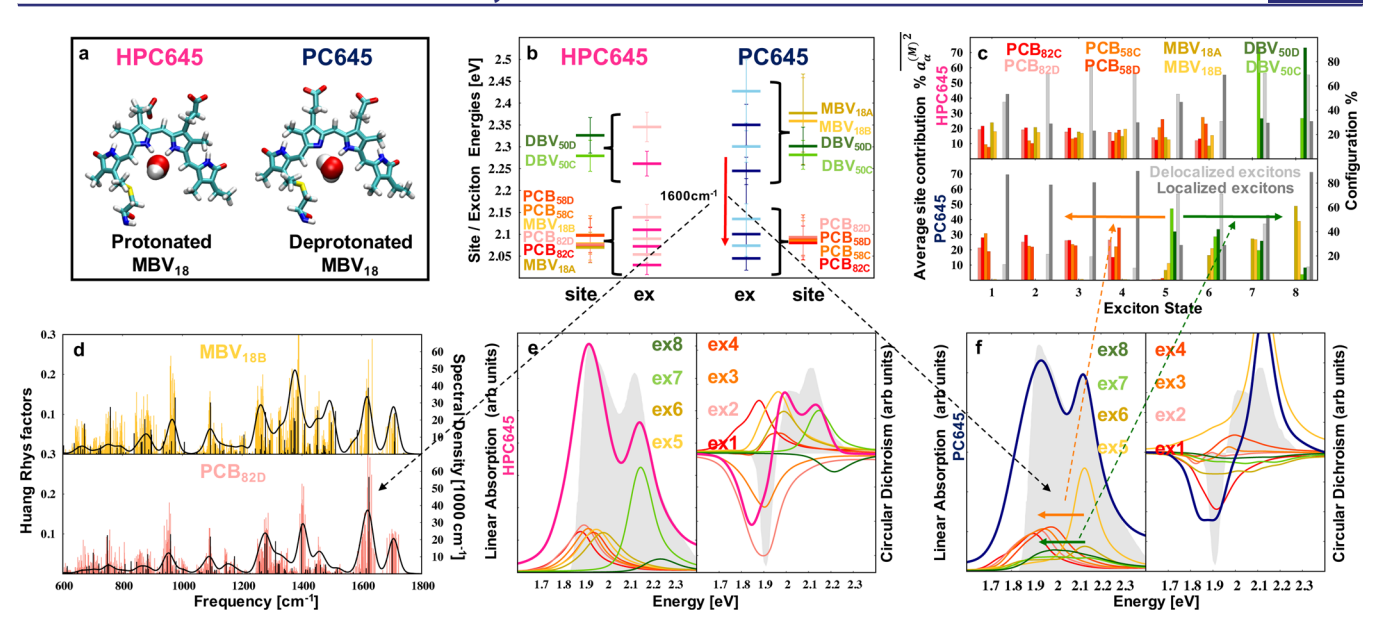


Figure 3. (a) Structures of protonated and unprotonated MBV₁₉ chromophores from the HPC645 and PC645 complexes, respectively. (b) Far left and far right horizontal bars give mean site energies for chromophores color coded consistently with structures in Figure 1 for HPC645 and PC645 respectively. Error bars indicate standard deviation of fluctuations in the site energies in the Hamiltonian ensembles. Pink and blue horizontal bars in the central section of this panel give mean eigenvalues of exciton Hamiltonians or exciton energies for HPC645 and PC645 complexes, respectively. Error bars again give standard deviations of exciton energy fluctuations. (c) Exciton state ensemble average compositions and localization characteristics. For each exciton the color coded left bars give the average populations of the different chromophore site states (left axis scale), while the right-hand dark-gray and light-gray bars give the fraction of ensemble members that have localized/delocalized eigenstates as specified by the right axis scale. (d) Average intramolecular spectral densities for bilins DBV_{50D}, MBV_{18B}, PCB_{58D}, and PCB_{82D}. Note scale changes in left and right subpanels. (e) Absorption (left) and CD spectrum (right) for HPC645 complex at T = 298 K. Simulated linear absorption spectrum for HPC645 (pink) compared with the experimentally measured spectrum at room temperature (filled gray). In addition, the average excitonic contributions to the overall computed spectra are shown with colored lines. (f) Same as panel (e) only now for the unprotonated PC645 complex. Arrows are drawn to scale representing the 1600 cm⁻¹ transition between exciton states in which the electronic excitation migrates from the donor state delocalized on the DBV₅₀ molecules to some localized acceptor state, e.g., in the orange band representing exciton state 3, which may involve localized excitation of, e.g., a PCB_{82D} molecule, or the green band representing exciton state 8, which may involve localized excitation of, e.g., an MBV₁₈₈ molecule. Electronic de-excitation to these lower energy states is accompanied by excitation of a 1600 cm⁻¹ strongly coupled vibrational mode apparent in our calculated spectral densities for these chromophores associated with their $\nu = 1 \leftarrow 0$ vibrational excitations.

and DBV_{19} chromophores that collectively give rise to same-signed exciton rotatory strength. Exciton 8, on the other hand, contributes negligibly to the CD signal because the variation in the site combinations gives rise to positive and negative signals that cancel each other. The overall resulting signs for the remaining exciton states are elusive. From configuration to configuration, the intensity and the sign of the computed excitonic rotatory strength alternate due to many factors such as the sign of the excitonic magnetic strength and/or the sign of the expansion coefficients.

Analysis of PC645 Results. The protein backbone and the bilin binding sites for the PC645 complex are very similar to those in PE545, but as outlined earlier, PC645 binds pairs of DBV₅₀, PCB₅₈, PCB₈₂, and MBV₁₈ chromophores (see Figure 1). The organisms from which the PC645 light harvesting complexes are derived live in environments where longer wavelength light predominates compared to those that use PE545 so they incorporate these longer wavelength absorbing chromophores in essentially the same protein scaffold. Thus, the DBV chromophores that were at the bottom of the funnel (position 19) in PE545 are now, in PC645, at the top in the source position 50 at the dimer interface. As explored below, precisely which position behaves as the overall "sink" state in the PC645 complex is influenced by the protonation state of molecules at peripheral site 18, and this observation suggests an interesting pathway control mechanism.

Similar to PE545, the two central nitrogens, NB and NC, in the B and C pyrrole rings of the DBV₅₀, PCB₅₈, and PCB₈₂ bilins are coordinated to aspartic acid residues, and these titratable sites are hence assumed to be protonated. The remaining DBV₁₉ bilins in PE545 and MBV₁₈ chromophores in PC645 are uniquely coordinated to a water molecule. In the PE545 system, however, the water molecule is also coordinated with a nearby histidine such that the relative orientation of the histidine and water molecules (see Supporting Information) from well resolved X-ray crystal structure data suggests protonation of both the central nitrogen atoms of the DBV₁₉ chromophores. This fully protonated structure was used in the calculations reported in the previous section. The water molecules near the MBV₁₈ binding sites in PC645, on the other hand, do not show any clear additional coordination to the neighboring residues. As presented in the Supporting Information, the unknown relative orientation of these water molecules opens up the possibility of different protonation states of the MBV_{18} bilins in PC645. 95,96 Thus, in this section we report the results of two separate studies of the PC645 complex: one involving the protonated forms of both MBV_{18A} and MBV_{18B}, and another study in which the unprotonated forms (see Figure 3a) have been considered. In the discussion that follows, the complex with all eight bilins in their fully protonated forms will be referred to as HPC645; the complex with protonated DBV₅₀, PCB₅₈, and PCB₈₂ chromophores, but unprotonated NB MBV_{18} chromophores, will be referred to as PC645.

In Figure 3b, (and also tabulated in the Supporting Information) the averaged site energies with the standard deviations computed from more than 300 inherent structure configurations sampled from more than 40 ns of molecular dynamics are presented together with the resulting averaged exciton energies for both HPC645 and PC645. In HPC645, the site energies form two distinct bands in which the higher energy band is composed of the central pair of DBV₅₀ chromophores. The lower energy band includes the six remaining excited states of the longer π -conjugated PCB and MBV bilin chromophores. Similar to PE545, asymmetrical mean site energies are computed for the central pair in HPC645, where the site excitation energy for DBV_{SOD} is on average larger than the complementary DBV_{50C} site energy over the duration of our sampling run. Due to both large site energy differences between the higher energy DBV chromophores and the other six lower energy sites in HPC645, as well as the large electronic coupling (\sim 200 cm⁻¹) between the DBV₅₀ bilins, the two highest exciton states (7 and 8) for this fully protonated complex are predominantly delocalized over the two DBV₅₀ chromophores, as shown in the upper panel of Figure 3c.

The remaining six bilins in HPC645 have near-degenerate mean site energies, with the average PCB58 site energies being only ~0.01 eV above those of the PCB82 and MBV19 chromophores. From Figure 3c we find that the six resulting exciton states that form the lower band are significantly delocalized in the majority of sampled configurations, with the exception of exciton state 6. In approximately 70% of the configurations, exciton 6 is a localized excited state, where the site that is electronically excited will depend on the configuration-dependent relative site energy gaps and ordering between the PCB and MBV sites. The lower energy exciton states are generally delocalized and involve mixing of excitation on the PCB₅₈ and MBV₁₈ chromophores or between the PCB₈₂ and MBV₁₈ chromophores, and very little delocalization involving mixing of the PCB58 and PCB82 chromophores is observed due to very weak electronic coupling between these bilins.

In the unprotonated PC645 complex, on the other hand, the computed site energies suggest that the removal of a proton from one of the central pyrrole rings leads to a significant increase, ~0.3 eV, in the average vertical transition energies for the MBV₁₈ bilins. Though the equilibrium configurations remain relatively unaffected by the deprotonation, the increase in excitation energy can be explained in terms of the molecular orbital analysis presented in the Supporting Information (see Figure S3). As presented in Figure 3b, the unprotonated MBV chromophores in the PC645 complex in fact have larger site energies, on average, than those of the DBV50 chromophores, but they fluctuate significantly such that the site energy ordering between these two pairs of bilins vary from configuration to configuration. This change in the MBV₁₈ site energies leads to significantly different exciton states in the unprotonated PC645 complex. Unlike HPC645, the upper exciton band in PC645 is thus composed of four eigenstates that are either localized or delocalized on the DBV₅₀ central pair and on the MBV₁₈ chromophores. The bottom panel in Figure 3c indicates that exciton state 8 is most often a localized state involving excitation of MBV_{18} chromophores. The character of exciton states 7 through 5 in PC645 varies from configuration to configuration. Of these states, exciton state 5

most closely resembles the constructively delocalized DBV $_{50}$ states observed in the HPC645 complex. The remaining exciton states 4 through 1 in PC645 are predominantly localized excited states where the localization alternates between the PCB $_{58}$ and PCB $_{82}$ chromophores.

In addition to the significant differences in site and exciton energies between the HPC645 and PC645 complexes outlined above, deprotonation also has a considerable effect on system bath interactions, in terms of both total reorganization energies reported in the Supporting Information and local chromophore spectral densities. When all bilins are in their protonated forms (HPC645), the total reorganization energies and the shape of the spectral densities (see the Supporting Information for details) are very similar to those presented for the PE545. In PC645, on the other hand, the amplitude of the spectral density of the unprotonated MBV₁₈ chromophores increases drastically, reflecting the large increase of average total reorganization energy from $\sim 1550 \text{ cm}^{-1}$ in HPC645 to 4200-4400 cm⁻¹ in PC645. Interestingly, spectral density peaks for PCB_{82D} are also slightly amplified, resulting in an increase in its mean total reorganization energy by ~400 cm⁻¹ (~20%) suggesting that a nonlocal correlated protein (allosteric) reorganization process may be at work upon MBV deprotonation.

The computed linear absorption and circular dichroism spectra are shown in Figure 3e and Figure 3f for HPC645 and PC645 respectively. Unlike PE545 where the computed spectra were *not* shifted to align with the experimental measurements, computed spectra for both HPC645 and PC645 have been uniformly blue-shifted by 0.06 eV to best match the experimentally observed spectral peaks (shown as filled-gray). This relatively small shift (<500 cm⁻¹) could arise from the limitations of the SOS-CIS(D) electronic structure method, $^{97-100}$ or the QM/MM scheme adopted in these calculations, but may also have a significant component coming from the approximate treatment of the electronic-nuclear interactions in the Redfield-like theory used to compute the line shapes. In the experiment, the absorption spectrum shows two main peaks at approximately 2.12 and 1.91 eV. The computed spectra for both the HPC645 and PC645 complexes capture the relative energy difference between the two main spectral features, but with different relative intensities. These similarities and differences can be understood by analyzing the different excitonic contributions as presented in the left panels of Figure 3e and Figure 3f.

The analysis in the case of the protonated HPC645 spectrum is straightforward. The peak at 2.12 eV mainly results from exciton states 7 and 8, where the relative absorption intensities of these excitons are consistent with prototypical intensity redistribution in which the lower energy, "constructive" linear combination of the DBV₅₀ sites leads to higher oscillator strength of the DBV+ delocalized exciton state and the higher energy, "destructive" linear combination leads to a less intense, nearly dark absorption feature associated with the DBV_ state. The remaining six exciton states in the case of HPC645 give rise to the higher intensity peak at 1.91 eV. Each of these six exciton states have smaller oscillator strength than exciton 7 due to disorder in the delocalization length and site composition for each configuration. In the unprotonated PC645 complex, on the other hand, only four exciton states contribute to absorption near 1.91 eV and, thus, the intensity of this lower energy absorption peak decreases relative to that observed for the HPC645 complex. The peak at 2.12 eV in the unprotonated PC645 complex is mainly attributed to exciton

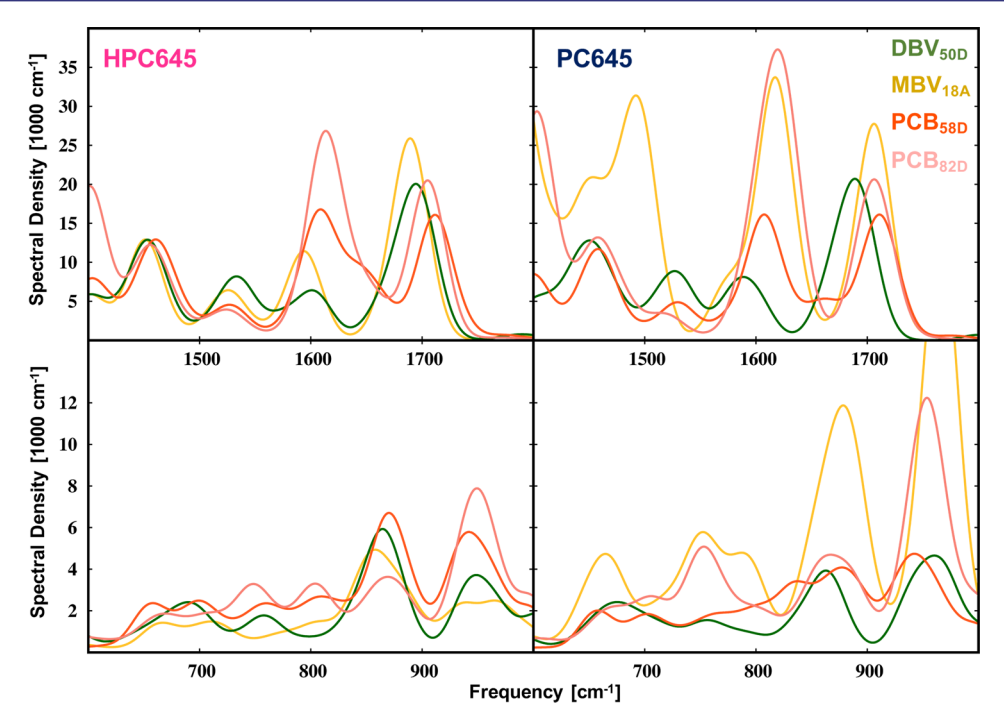


Figure 4. Upper panels show average computed spectral densities for various chromophores for HPC645 and PC645 in the range 1400–1800 cm⁻¹. The lower panels show similar results for the range 600–1000 cm⁻¹. A detailed presentation of all computed spectral densities is given in the Supporting Information in Figure S5.

state 5, and this state closely resembles exciton 7 in HPC645, i.e. the in-phase combination of the DBV_{50} sites, as discussed above.

The remaining exciton states, 6, 7, and 8 for the unprotonated PC645 complex have very broad absorption profiles and give a background that selectively enhances the absorption peak at 2.12 eV. As detailed in the Supporting Information the position and shapes of these absorption features, within the framework of the Redfield theory approximations, result from instantaneous bath relaxation that red-shifts the exciton absorption peaks centered at the vertical transition energies by the corresponding exciton reorganization energies. Thus, the absorption line shapes are built out from the "adiabatic" $0 \rightarrow 0$ transition energies. The absorption profiles for exciton states 6 through 8, involving the strongly fluctuating excited MBV bilins with large reorganization energies, are influenced by both static disorder and strong electronicvibrational interactions leading to these broad features that are ultimately centered around higher energies in the case of PC645 so as to capture more closely the relative partitioning of intensity of the different bands when compared to the experimental results. These bands, however, are generally excessively broadened to lower energies due to most likely the limitations of the simple line shape theory employed in these

These problems of excessive broadening also make the computation of the more sensitive CD signals a significant challenge. Thus, for example, the artificial broadening of the signed CD components arising from the higher energy excitons overlap excessively with different signed contributions at lower energies, causing inaccurate cancellations, making the computation of the CD spectrum very sensitive. Nevertheless, the position of the zero crossing point relative to the experimental results, and the "positive-high" and "negative-low" energy features apparent in the experiment are reproduced in the

computed CD spectra for both HPC645 and PC645. A more detailed discussion of the breakup of the CD spectra into component exciton signals is presented in the Supporting Information.

The general reliability of our first-principles model Hamiltonian ensemble calculations is highlighted when we use the results in Figure 3 to interpret recently published experimental observations of excited state wave packet dynamics for the PC645 system from the Scholes Laboratory. 101 The experimental results, depicted, for example, in the antidiagonal cut from the 2DES results in Figure 2 of the recent work of Dean et al., ¹⁰¹ are interpreted as arising from direct resonant energy transfer from the higher energy delocalized DBV+ exciton state, at the core of the complex, to vibronically excited states localized on the peripheral chromophores. To definitively assign vibrational modes and determine the origins of the relatively long-lived coherences observed in these types of experiments, explicit dynamical studies employing our model Hamiltonian ensemble are required and are beyond the scope of the current report. However, we hypothesize that the 1600 cm⁻¹ oscillatory feature probably arises from dynamical interplay between exciton 5 in Figure 3f and the lower localized PCB exciton states, or it could also arise from coupling to the vibronic states of exciton 8 in PC645 as indicated by the orange and green arrows in Figure 3c, respectively. The premise for this hypothesis lies in the absorption spectrum presented in Figure 3f, where, as previously discussed, the peaks correspond to the "adiabatic"like excitation, or the $0\rightarrow 0$ pure electronic transition energies. From the mean peak position for exciton 5, the energy difference to the lower exciton states localized on the PCBs is approximately 1600 cm⁻¹, as demonstrated with the orange arrow. With the vibrational excitation of a PCB vibrational mode of frequency 1600 cm⁻¹, the direct, resonant energy transfer from the higher exciton state to the final acceptor state

could occur. This vibrational excitation is further validated by the relatively large Huang–Rhys factors computed for PCB_{82D} bilin where modes in the vicinity of 1600 cm⁻¹ have the largest Huang–Rhys factors with a magnitude greater than 0.2 as presented in Figure 3d.

From the bottom panel of Figure 3c we see that in \sim 70% of our sampled Hamiltonians, exciton 5 is delocalized (light gray bar, right axis) involving coherent superpositions of mainly DBV chromophores (green bars), forming the DBV₊ delocalized exciton, consistent with the experimental assignment. However, for the possible final states, e.g. excitons 1-4 (red-orange), or exciton 8 (forest green), ~90% of the sampled Hamiltonians show strong localization (dark gray bars) of these potential acceptor states. From Figure 3c we see that excitons 1-4 are localized on the different PCB molecules, while exciton 8 fluctuates between localized excitation of the MBV₁₈ chromophores. From the absorption spectrum contributions shown in Figure 3f, exciton 8 involves MBV₁₈ chromophores whose excitation energies are significantly red-shifted and broadened due to the large reorganization energies of these unprotonated chromophores in the PC645 complex.

The representative computed spectral densities and Huang—Rhys factors displayed in Figure 3d, and detailed in Figure S5 in the Supporting Information, can help to understand microscopic factors that influence excitation energy relaxation processes. This panel presents the averaged Gaussian broadened spectral densities of both the MBV₁₈ and PCB₈₂ chromophores and the Huang—Rhys factors of the different modes for our entire computed ensemble of Hamiltonians for the unprotonated PC645 complex. These results give an indication of the dispersion underlying the averages.

In Figure 4 we explore the influence of deprotonation on different regions of our average spectral densities for the various chromophores that may be significant for enhancing the resonant interchromophore energy transfer. From the upper panels of this figure it is clear that deprotonation of the MBV₁₈ molecules, taking us from HPC645 (left) to PC645 (right), has little effect on the vibrational modes near ~1700 cm⁻¹, for example, for all the chromophores (there is, however, a small blue shift for this mode on MBV_{18A}). For the \sim 1600 cm⁻¹ modes, on the other hand, the DBV₅₀ and PCB₅₈ chromophores show essentially no change, but the spectral density for this mode on the deprotonated MBV_{18A} molecule increases by more than 3-fold. Remarkably, deprotonating the MBV₁₈ molecules causes the spectral density of the 1600 cm⁻¹ mode of the PCB₈₂ molecule to increase by nearly 50%, consistent with the allosteric behavior mentioned earlier. These same sorts of changes are observed for the 600-1000 cm⁻¹ region of the spectral densities presented in the lower panels of Figure 4 where we observe that the electronic-vibrational coupling of the \sim 850 and \sim 950 cm⁻¹ features of the MBV₁₈ chromophore increases by roughly 3-fold and the ~950 cm⁻¹ feature of the PCB₈₂ chromophore again increases by about

These observations suggest that deprotonation of the MBV_{18} molecules can tune the electronic—vibrational coupling at specific frequencies to control dissipation to make the MBV_{18} and PCB_{82} molecules the dominant acceptor chromophores, so deprotonation may control the pathway that excitation energy takes as it flows through this pigment—protein complex. Thus, our model Hamiltonian ensemble enables interpretation of the experimental results; ¹⁰¹ in particular, our calculations suggest that as the electronic excitation moves from the DBV_{50}

chromophores of the delocalized exciton 5 donor to the localized MBV_{18} chromophores of exciton 8, the strongly coupled $1600~\rm cm^{-1}$ mode of an MBV_{18} acceptor may be excited as a result of the enhanced coupling due to deprotonation. The involvement of the PCB_{82} chromophore as an excitation energy acceptor may also occur due to enhanced couplings on MBV_{18} deportation, so both these pathways may favor the excitation of coherent vibronic wave packets involving the $1600~\rm cm^{-1}$, consistent with the experimental results.

Our calculated spectral densities for the MBV₁₈ and PCB₈₂ chromophores also show enhanced features for modes with other vibrational frequencies; for example, there are strong peaks near \sim 1300, \sim 1400, and \sim 1500 cm⁻¹ that are also enhanced by deprotonation, as well as the features near ~850 cm⁻¹, and ~950 cm⁻¹ mentioned above. Given the broad excitonic bands that contribute to the linear absorption spectrum of Figure 3f, one might expect to be able to draw many different length arrows connecting states from under the donor exciton 5 peak, e.g., with other exciton acceptor states that involve resonance with these different strongly coupled vibrational modes. If the approximations underlying Förster resonance energy transfer theory are reliable, 73,101 the line shape of the emission spectrum will determine which acceptor states should be involved in energy transport. Our Hamiltonian ensemble approach can thus, in principle, be applied to compute these emission features and make predictions about energy transfer processes which can be benchmarked against accurate quantum dynamics calculations.

Other recent 2DES studies of phycobili pigment-protein systems have provided evidence of coherent energy transfer dynamics involving additional frequencies; for example, persistent oscillatory cross-peak features near 700 and 800-850 cm^{-1102,103} have been observed. The lower frequency feature has been assigned as purely electronic coherence between the two exciton states delocalized on the pair of DBV chromophores. The 800-850 cm⁻¹ feature, on the other hand, has been attributed 103 to excited state dynamics in the upper band of states, which our Hamiltonian ensemble calculations suggest are composed of the delocalized DBV states and the localized MBV states of the unprotonated PC645 complex. The strong inhomogeneous broadening of the states associated with excitons 7 and 8 may result in a significant number of configurations with $0 \rightarrow 0$ transition energy gaps near 800 cm⁻¹ between exciton states 5 and 7 or 5 and 8. The computed Huang-Rhys factors for the MBVs in this vicinity presented in Figure 3d are also large and suggest an assignment in agreement with experimental interpretations. Perhaps site energy fluctuations are correlated with the fluctuation of the spectral densities in this region; e.g., mode frequencies and couplings fluctuate concertedly to often bridge the exciton energy gap between states and facilitate resonant energy transfer. Such correlations are yet to be explored. Though these results are not yet perfect, it is clear that our approach for constructing these model Hamiltonian ensembles is very accurate and robust and that we are now in a position to begin to compute more detailed and accurate quantum dynamical responses that can be predictive and probe in ultrafast spectroscopies using these first-principles model Hamiltonian ensemble methods as our guide to detailed molecular interpretation.

■ CONCLUSIONS AND OUTLOOK

We have presented a highly accurate first-principles protocol for generating ensembles of realistic model Hamiltonians that may be subsequently used in excited-state dynamical simulations of multichromophore light harvesting systems. Under the assumption that the exciton dynamics occurs rapidly on the time scale of molecular rearrangement of the local inherent structures, electronic properties for each QM/MM optimized inherent structure were computed to simulate unique spectral features that overall give rise to the inhomogeneous broadening. This Hamiltonian ensemble approach thus enables us to go beyond the more standard phenomenological schemes that make the opposite, often unrealistic assumption that the environment moves quickly from basin to basin on the time scale of the excitation energy relaxation processes of interest, suggesting that an averaged Hamiltonian can be used to describe the excitation dynamics. To obtain reliable results this approach must often be augmented by including a phenomenological description of fluctuations, for example, by averaging dynamical results over a Gaussian distribution of site energies, the properties of which are usually determined by fitting to experiments. Our first-principles Hamiltonian ensemble approach completely avoids the ambiguities of these phenomenological schemes, and importantly, it should include a realistic estimate of any correlation that may exist between fluctuations in components of the system Hamiltonian or correlations in system-bath couplings. To date there have been attempts 104-107 to explore such correlations, but due to the limited accuracy of the methods employed in these earlier studies, little evidence of such correlation has been observed. We believe the computational methodology presented here is now sufficiently accurate to explore the possibility of correlations in protein and chromophore motions enabling long-lived excitonic coherence in terms of which many 2DES experiments on light harvesting systems have been discussed. Analysis of our model Hamiltonian ensemble studying these correlations is currently ongoing.

For the phycobiliprotein systems we have studied here we have seen that, from configuration to configuration, site energies and site energy ordering of the chromophores fluctuate significantly and give rise to highly configurationdependent excitonic energies and states that change in delocalization length and site composition. Considerable fluctuations are also observed in the magnitude of the frequency-dependent electronic-nuclear couplings where the total intramolecular reorganization energies vary by several hundreds of wavenumbers. These strong fluctuations in the excited state properties reflect the unique nature of the bilin chromophores, where the electronic densities and energies are highly sensitive to the slight changes in the torsional twist about the methine bond bridging the pyrrole rings. How much the pathways and rates for each inherent structure differ about the ensembled-averaged dynamics, as well as the reliability of extracted dynamical observables computed from the ensembleaveraged Hamiltonians, is currently being explored.

With reliable electronic structure methods, we have demonstrated that we can not only predict relative positions of absorption spectrum peaks of the PE545 and PC645 systems, but these methods are sufficiently accurate to compute absolute excitation energies and even start to resolve spectroscopic differences arising from conformational fluctuations and changes in chromophore protonation state. These

systems highlight the diversity found in nature, where, though the protein scaffold and the geometrical arrangement of the same number of chromophores are highly conserved, simply tuning the double-bonded topology of the chromophores leads to large changes in the excited state energy landscape. In PE545, the chromophore composition is not as diverse as in PC645 and, consequently, the exciton energy gaps are on average much smaller in comparison. This suggests that in PE545, in contrast to previous studies, energy transfer and relaxation probably do not actively involve the high-frequency intramolecular modes for many of the configurations in the ensemble, but rather, lower frequency chromophore vibrations and protein and solvent modes can drive dissipative relaxation from higher to lower energy exciton states in this system.

Our calculations predict that the opposite situation holds for the PC645 complex, where in general the mean exciton energy gap between the higher exciton band to the lower band is large, suggesting that the only way to meet the resonant energy transfer criteria is through the dynamical interplay of the vibronic states involving the high-frequency intramolecular vibrational coordinates. The small change in the pigmentprotein configuration induced by the simple removal of a proton leads to completely different excited state properties, where independent of whether the MBV is protonated or not our calculations reveal that the highest exciton state of PC645 is a delocalized state involving excitation of the two DBV molecules at the center of the protein dimer interface. For the unprotonated MBV system, our model Hamiltonian ensemble predicts that most of the lower energy states that are typically ~1600 cm⁻¹ below this highest delocalized excited state are actually localized, while for the protonated MBV complex, on the other hand, most of the lower energy exciton states are delocalized. The fact that the calculated spectral densities give strong couplings for modes with precisely the right frequencies to match up with our calculated interchromophore energy transfer transitions, and these results also coincide very closely with recent ultrafast 2DES experimental observations, 101,102 is suggestive that our model Hamiltonian ensemble will be able to be used in more complete dissipative quantum dynamics calculations of nonlinear spectroscopy signals, beyond the simple lifetime broadening theory results reported here. Remarkably, our calculations suggest that the character of the acceptor states changes significantly as a result of simply protonating or deprotonating the MBV chromophores. Functionally the localized peripheral states that result on deprotonation may enable focusing of the energy transfer pathway onto individual molecules to make the next steps in moving the excitation energy toward the reaction center more efficient. Studies of these types of localization/delocalization patterns in our Hamiltonian ensemble will be important for using this approach to understand how fluctuations in the ensemble enable efficient light harvesting pathways.

ASSOCIATED CONTENT

Supporting Information

The Supporting Information is available free of charge on the ACS Publications website at DOI: 10.1021/jacs.7b01780.

Summary of computational details including the following: MD simulations, electronic structure calculations of chromophore site energies, interchromophore electronic couplings, intramolecular spectral densities, the non-Markovian reduced density matrix theory of

lifetime broadening used in our spectral line shape calculations, and an analysis of calculated CD spectra. Supplementary figures include the following: study of local coordination environment of DBV₁₉ and MBV₁₈ in PE545 and PC645, simple electronic structure models of effects of protonation on MBV₁₈ excitation energies, schematic exciton coupling maps exploring exciton localization, and a summary figure showing fluctuations in exciton Hamiltonian ensemble and different calculations of absorption and CD spectra. Supplementary tables include the following: mean chromophore site energies, electronic couplings and reorganization energies and their fluctuations. Optimized geometries that sample the inherent structure ensembles for the studied complexes will be made available upon request. (PDF)

AUTHOR INFORMATION

Corresponding Author

*coker@bu.edu

ORCID ®

David F. Coker: 0000-0001-6210-5228

Notes

The authors declare no competing financial interest.

ACKNOWLEDGMENTS

We gratefully acknowledge support for this research from the National Science Foundation under Grant Number CHE-1301157. We acknowledge the computational resources provided by Boston University's Office of Research Computing, Information Systems and Technology.

REFERENCES

- (1) Ginsberg, N. S.; Cheng, Y.; Fleming, G. R. Acc. Chem. Res. 2009, 42, 1352–1363.
- (2) Jonas, D. M. Annu. Rev. Phys. Chem. 2003, 54, 425-463.
- (3) West, B. A.; Moran, A. M. J. Phys. Chem. Lett. 2012, 3, 2575–2581.
- (4) Milota, F.; Sperling, J.; Nemeth, A.; Mancal, T.; Kauffmann, H. F. Acc. Chem. Res. **2009**, 42, 1364–1374.
- (5) Brixner, T.; Stenger, J.; Vaswani, H. M.; Cho, M.; Blankenship, R. E.; Fleming, G. R. *Nature* **2005**, 434, 625–628.
- (6) Chenu, A.; Scholes, G. D. Annu. Rev. Phys. Chem. 2015, 66, 69-96.
- (7) Cina, J. A.; Kovac, P. A.; Dean, C. C. J. J. C.; Scholes, G. D. J. Chem. Phys. **2016**, 144, 175102–175120.
- (8) Arpin, P. C.; Turner, D. B.; McClure, S. D.; Jumper, C. C.; Mirkovic, T.; Challa, J. R.; Lee, J.; Teng, C. Y.; Green, B. R.; Wilk, K. E.; Curmi, P. M. G.; Hoeff-Emden, K.; McCamant, D. W.; Scholes, G. D. J. Phys. Chem. B 2015, 119, 10025–10034.
- (9) McClure, S. D.; Turner, D. B.; Arpin, P. C.; Mirkovic, T.; Scholes,G. D. J. Phys. Chem. B 2014, 118, 1296-1308.
- (10) Tiwari, V.; Peters, W. K.; Jonas, D. M. Proc. Natl. Acad. Sci. U. S. A. 2013, 110, 1203–1208.
- (11) Doust, A. B.; van Stokkum, I. H. M.; Larsen, D. S.; Wilk, K. E.; Curmi, P. M. G.; van Grondelle, R.; Scholes, G. D. *J. Phys. Chem. B* **2005**, *109*, 14219–14226.
- (12) Novoderezhkin, V. I.; Doust, A. B.; Curutchet, C.; Scholes, G. D.; van Grondelle, R. *Biophys. J.* **2010**, *99*, 344–352.
- (13) Novoderezhkin, V. I.; van Grondelle, R. Phys. Chem. Chem. Phys. **2010**, 12, 7352–7365.
- (14) Marin, A.; Doust, A. B.; Scholes, G. D.; Wilk, K. E.; Curmi, P. M. G.; van Stokkum, I. H. M.; van Grondelle, R. *Biophys. J.* **2011**, *101*, 1004–1013.

- (15) Turner, D. B.; Dinshaw, R.; Lee, K.; Belsley, M. S.; Wilk, K. E.; Curmi, P. M. G.; Scholes, G. D. *Phys. Chem. Chem. Phys.* **2012**, *14*, 4857–4874.
- (16) Richards, G. H.; Wilk, K. E.; Curmi, P. M. G.; Quiney, H. M.; Davis, J. A. J. Phys. B: At., Mol. Opt. Phys. 2012, 45, 154015–154023.
- (17) Schlau-Cohen, G. S.; Calhoun, T. R.; Ginsberg, N. S.; Read, E. L.; Ballottari, M.; Bassi, R.; van Grondelle, R.; Fleming, G. R. *J. Phys. Chem. B* **2009**, *113*, 15352–15363.
- (18) Harel, E.; Engel, G. S. Proc. Natl. Acad. Sci. U. S. A. 2012, 109, 706-711.
- (19) Holdaway, D. I. H.; Collini, E.; Castro, A. O. J. Chem. Phys. **2016**, 144, 194112–194136.
- (20) Fleming, G. R.; Schlau-Cohen, G. S.; Amarnath, K.; Zaks, J. Faraday Discuss. **2012**, 155, 27–41.
- (21) Chen, M.; Blankenship, R. E. Trends Plant Sci. 2011, 16, 427-431.
- (22) Perrine, Z.; Negi, S.; Sayre, R. T. Algal Res. 2012, 1, 134-142.
- (23) Kamran, M.; Delgado, J. D.; Friebe, V.; Aartsma, T. J.; Frese, R. N. *Biomacromolecules* **2014**, *15*, 2833–2838.
- (24) Alharbi, F. H.; Kais, S. Renewable Sustainable Energy Rev. 2015, 43, 1073–1089.
- (25) Hedley, G. J.; Ruseckas, A.; Samuel, I. D. W. Chem. Rev. 2017, 117, 796–837.
- (26) Bredas, J.; Sargent, E. H.; Scholes, G. D. Nat. Mater. 2016, 16, 35–44.
- (27) Wasielewski, M. R. Acc. Chem. Res. 2009, 42, 1910-1921.
- (28) Schlau-Cohen, G. S.; Wang, Q.; Southall, J.; Cogdell, R. J.; Moerner, W. E. *Proc. Natl. Acad. Sci. U. S. A.* **2013**, *110*, 10899–10903.
- (29) Uchiyama, D.; Hoshino, H.; Otomo, K.; Onda, T.; Wanatabe, A.; Oikawa, H.; Fujiyoshi, S.; Matsushita, M.; Nango, M.; Wanatabe, N.; Sumino, A.; Dewa, T. *Chem. Phys. Lett.* **2011**, *511*, 135–137.
- (30) Schlau-Cohen, G. S.; Bockenhauer, S.; Wang, Q.; Moerner, W. E. Chem. Sci. 2014, 5, 2933.
- (31) Schlau-Cohen, G. S.; Wang, Q.; Southall, J.; Cogdell, R. J.; Moerner, W. E. *Proc. Natl. Acad. Sci. U. S. A.* **2013**, *110*, 10899–10903.
- (32) Schlau-Cohen, G. S.; Ishizaki, A.; Fleming, G. R. Chem. Phys. **2011**, 386, 1–22.
- (33) Skochdopole, N.; Mazziotti, D. A. J. Phys. Chem. Lett. 2011, 2, 2989–2993.
- (34) Huo, P.; Coker, D. F. In Chapter 8 Excitation Energy Transfer in Light-Harvesting Systems: Theory, Models, and Application; Burghardt, I., Haacke, S., Eds.; Pan Stanford Publishing: Singapore, 2017.
- (35) Mukamel, S. Annu. Rev. Phys. Chem. 2000, 51, 691-729.
- (36) Cheng, Y.; Fleming, G. R. Annu. Rev. Phys. Chem. 2009, 60, 241–262.
- (37) Ishizaki, A.; Fleming, G. R. J. Chem. Phys. 2009, 130, 234111–234121.
- (38) Ishizaki, A.; Fleming, G. R. Proc. Natl. Acad. Sci. U. S. A. 2009, 106, 17255–17260.
- (39) Ishizaki, A.; Tanimura, Y. J. Phys. Soc. Jpn. 2005, 74, 3131-3134.
- (40) Beck, M. H.; Jackle, A.; Worth, G. A.; Meyer, H. D. Phys. Rep. **2000**, 324, 1–105.
- (41) Schulze, J.; Shibl, M. F.; Al-Marri, M. J.; Kuhn, O. J. Chem. Phys. **2016**, 144, 185101–185111.
- (42) Bruning, C.; Engel, V. Chem. Phys. 2017, 482, 64-68.
- (43) Berkelbach, T. C.; Markland, T. E.; Reichman, D. R. J. Chem. Phys. **2012**, 136, 084104–084115.
- (44) Huo, P.; Coker, D. F. J. Chem. Phys. 2011, 135, 201101–201105.
- (45) Doust, A. B.; Marai, C. N. J.; Harrop, S. J.; Wilk, K. E.; Curmi, P. M. G.; Scholes, G. D. *J. Mol. Biol.* **2004**, 344, 135–153.
- (46) Wlodarczyk, L. M.; Snellenburg, J. J.; Ihalainen, J. A.; van Grondelle, R.; van Stokkum, I. H. M.; Dekker, J. P. *Biophys. J.* **2015**, *108*, 261–271.
- (47) Hayes, D.; Engel, G. S. Biophys. J. 2011, 100, 2043-2052.
- (48) Renger, T.; Mueh, F. Phys. Chem. Chem. Phys. 2013, 15, 3348-3371.
- (49) Jurinovich, S.; Viani, L.; Curutchet, C.; Mennucci, B. *Phys. Chem. Chem. Phys.* **2015**, *17*, 30783–30792.

- (50) Cole, D. J.; Chin, A. W.; Hine, N. D. M.; Haynes, P. D.; Payne, M. C. J. Phys. Chem. Lett. **2013**, 4, 4206–4212.
- (51) Curutchet, C.; Mennucci, B. Chem. Rev. 2017, 117, 294-343.
- (52) Brunk, E.; Rothlisberger, U. Chem. Rev. 2015, 115, 6217-6263.
- (53) Tavernelli, I. Acc. Chem. Res. 2015, 48, 792-800.
- (54) Gelin, M. F.; Sharp, L. Z.; Egorova, D.; Domcke, W. J. Chem. Phys. **2012**, 136, 034507–034520.
- (55) Chernyak, V.; Zhang, W. M.; Mukamel, S. J. Chem. Phys. 1998, 109, 9587-9601.
- (56) Toutounji, M. J. Chem. Phys. 2005, 123, 244102-244110.
- (57) de Bree, P.; Wiersma, D. A. J. Chem. Phys. 1979, 70, 790-801.
- (58) Zhang, L.; Silva, D.; Yan, Y.; Huang, X. J. Comput. Chem. 2012, 33, 1969–1980.
- (59) Kaminski, S.; Daminelli, G.; Mroginski, M. A. J. Phys. Chem. B **2009**, 113, 945–958.
- (60) Do, H.; Troisi, A. Phys. Chem. Chem. Phys. 2015, 17, 25123–25132.
- (61) Kim, C. W.; Rhee, Y. M. J. Chem. Theory Comput. 2016, 12, 5235-5246.
- (62) Kim, C. W.; Park, J. W.; Rhee, Y. M. J. Phys. Chem. Lett. 2015, 6, 2875–2880.
- (63) Li, Z.; Kermode, J. R.; De Vita, A. Phys. Rev. Lett. 2015, 114, 096405-096410.
- (64) Makhov, D. V.; Glover, W. J.; Martinez, T. J.; Shalashilin, D. V. J. Chem. Phys. **2014**, *141*, 054110-054121.
- (65) Hutter, J. J. WIREs Comput. Mol. Sci. 2012, 2, 604-612.
- (66) Lee, M. K.; Coker, D. F. J. Phys. Chem. Lett. 2016, 7, 3171–3178.
- (67) Stillinger, F. H.; LaViolette, R. A. J. Chem. Phys. 1985, 83, 6413–6418.
- (68) Wikfeldt, K. T.; Nilsson, A.; Pettersson, L. G. M. Phys. Chem. Chem. Phys. 2011, 13, 19918–19924.
- (69) Sumpter, B. G.; Meunier, V. J. Polym. Sci., Part B: Polym. Phys. **2012**, 50, 1071–1089.
- (70) Dror, R. O.; Dirks, R. M.; Grossman, J. P.; Xu, H.; Shaw, D. E. Annu. Rev. Biophys. **2012**, 41, 429–452.
- (71) Rosnik, A. M.; Curutchet, C. J. Chem. Theory Comput. 2015, 11, 5826-5837.
- (72) Kim, H. W.; Kelly, A.; Park, J. W.; Rhee, Y. M. J. Am. Chem. Soc. **2012**, 134, 11640–11651.
- (73) Blau, S. M.; Bennett, D. I. G.; Kreisbeck, C.; Scholes, G. D.; Aspuru-Guzik, A. arXiv: 1704.05449, *Phys. Chem.-Ph.***2017**.
- (74) Gao, J.; Shi, W.; Ye, J.; Wang, X.; Hirao, H.; Zhao, Y. *J. Phys. Chem. B* **2013**, *117*, 3488–3495.
- (75) Aghtar, M.; Strumpfer, J.; Olbrich, C.; Schulten, K.; Kleinekathofer, U. J. Phys. Chem. Lett. 2014, 5, 3131–3137.
- (76) Curutchet, C.; Novoderezhkin, V. I.; Kongsted, J.; Munoz-Losa, R. v. G.; Scholes, G. D.; Mennucci, B. J. Phys. Chem. B 2013, 117, 4263–4273.
- (77) Damjanovic, A.; Kosztin, I.; Kleinekathofer, U.; Schulten, K. Phys. Rev. E: Stat. Phys., Plasmas, Fluids, Relat. Interdiscip. Top. 2002, 65, 031919–03194.
- (78) Chandrasekaran, S.; Aghtar, M.; Valleau, S.; Aspuru-Guzik, A.; Kleinekathofer, U. J. Phys. Chem. B 2015, 119, 9995—10004.
- (79) Chandrasekaran, S.; Pothula, K. R.; Kleinekathofer, U. J. Phys. Chem. B 2017, 121, 3228-3236.
- (80) Daday, C.; Curutchet, C.; Sinicropi, A.; Mennucci, B.; Filippi, C. J. Chem. Theory Comput. 2015, 11, 4825–4839.
- (81) Gurunathan, P. K.; Acharya, A.; Ghosh, D.; Kosenkov, D.; Kaliman, I.; Shao, Y.; Krylov, A. I.; Slipchenko, L. V. J. Phys. Chem. B **2016**, 120, 6562–6574. PMID: 27314461.
- (82) Aghtar, M.; Kleinekathoefer, U.; Curutchet, C.; Mennucci, B. J. Phys. Chem. B **2017**, 121, 1330–1339.
- (83) Scholes, G. D.; Mirkovic, T.; Turner, D. B.; Fassioli, F.; Buchleitner, A. Energy Environ. Sci. 2012, 5, 9374–9393.
- (84) Harrop, S. J.; Wilk, K. E.; Dinshaw, R.; Collini, E.; Mirkovic, T.; Teng, C. Y.; Oblinsky, D. G.; Green, B. R.; Hoef-Emden, K.; Hiller, R. G.; Scholes, G. D.; Curmi, P. M. G. *Proc. Natl. Acad. Sci. U. S. A.* **2014**, 111, 2666–2675.

- (85) Huo, P.; Coker, D. F. J. Phys. Chem. Lett. 2011, 2, 825-833.
- (86) Mirkovic, T.; Doust, A. B.; Kim, J.; Wilk, K. E.; Curutchet, C.; Mennucci, B.; Cammi, R.; Curmi, P. M. G.; Scholes, G. D. *Photochem. Photobiol. Sci.* **2007**, *6*, 964–975.
- (87) Lee, M. K.; Huo, P.; Coker, D. F. Annu. Rev. Phys. Chem. 2016, 67, 639-668.
- (88) Viani, L.; Curutchet, C.; Mennucci, B. J. Phys. Chem. Lett. 2013, 4, 372–377.
- (89) Ratsep, M.; Freiberg, A. J. Lumin. 2007, 127, 251-259.
- (90) Pieper, J.; Freiberg, A. In Electron-Phonon and Exciton? Phonon Coupling in Light Harvesting, Insights from Line-Narrowing Spectroscopies; Golbeck, J., van der Est, A., Eds.; Springer: New York, 2014.
- (91) Renger, T.; Klinger, A.; Steinecker, F.; am Busch, M. S.; Numata, J.; Mueh, F. J. Phys. Chem. B 2012, 116, 14565–14580.
- (92) Andel, F., III; Murphy, J. T.; Haas, J. A.; McDowell, M. T.; van der Hoef, I.; Lugtenburg, J.; Lagarias, J. C.; Mathies, R. A. *Biochemistry* **2000**, *39*, 2667–2676.
- (93) Mroginski, M. A.; von Stetten, D.; Escobar, F. V.; Strauss, H. M.; Kaminski, S.; Scheerer, P.; Guenther, M.; Murgida, D. H.; Schmieder, P.; Bongards, C.; Gaertner, W.; Mailliet, J.; Hughes, J.; Essen, L.; Hildebrandt, P. *Biophys. J.* **2009**, *96*, 4153–4163.
- (94) Renger, T.; Marcus, R. A. J. Chem. Phys. 2002, 116, 9997-10019.
- (95) von Stetten, D.; Seibeck, S.; Michael, N.; Scheerer, P.; Mroginski, M. A.; Murgida, D. H.; Krauss, N.; Heyn, M. P.; Hildebrandt, P.; Borucki, B.; Lamparter, T. *J. Biol. Chem.* **2007**, 282, 2116–2123.
- (96) Escobar, F. V.; Lang, C.; Takiden, A.; Schneider, C.; Balke, J.; Hughes, J.; Alexiev, U.; Hildebrandt, P.; Mroginski, M. A. J. Phys. Chem. B 2017, 121, 47–57.
- (97) Rhee, Y. M.; Head-Gordon, M. J. Phys. Chem. A 2007, 111, 5314-5326.
- (98) Chibani, S.; Laurent, A. D.; Le Guennic, B.; Jacquemin, D. J. Chem. Theory Comput. **2014**, 10, 4574–4582.
- (99) Jacquemin, D.; Duchemin, I.; Blase, X. J. Chem. Theory Comput. **2015**, 11, 5340–5359.
- (100) Goerigk, L.; Grimme, S. J. Chem. Phys. 2010, 132, 184103–184112.
- (101) Dean, J.; Mirkovic, T.; Toa, Z.; Oblinsky, D.; Scholes, G. Chem. **2016**, 1, 858–872.
- (102) Turner, D. B.; Dinshaw, R.; Lee, K.; Belsley, M. S.; Wilk, K. E.; Curmi, P. M. G.; Scholes, G. D. Phys. Chem. Chem. Phys. **2012**, 14, 4857–4874.
- (103) Richards, G. H.; Wilk, K. E.; Curmi, P. M. G.; Davis, J. A. J. Phys. Chem. Lett. **2014**, 5, 43–49.
- (104) Hossein-Nejad, H.; Curutchet, C.; Kubica, A.; Scholes, G. D. J. Phys. Chem. B 2011, 115, 5243-5253.
- (105) Rancova, O.; Abramavicius, D. J. Phys. Chem. B 2014, 118, 7533-7540.
- (106) Bennett, D. I. G.; Amarnath, K.; Fleming, G. R. J. Am. Chem. Soc. 2013, 135, 9164–9173.
- (107) Sarovar, M.; Cheng, Y.; Whaley, K. B. Phys. Rev. E 2011, 83, 011906-011913.
- (108) Kolli, A.; O'Reilly, E. J.; Scholes, G. D.; Olaya-Castro, A. J. Chem. Phys. **2012**, 137, 174109–174121.